

# Importance of the Inter-Electrode Distance for the Electrochemical Synthesis of Magnetite Nanoparticles: Synthesis, Characterization, Computational Modelling, and Cytotoxicity

Seyedeh Maryam Dokht Taimoori and John F. Trant\*

*Department of Chemistry and Biochemistry, University of Windsor, Windsor, ON N9B 3P4, Canada*

Abbas Rahdar†

*Institute of Nano Science and Nano Technology, University of Kashan,  
Kashan, P. O. Box. 87317-51167, Islamic Republic of Iran and*

*Department of Physics, University of Zabol, Zabol,  
P. O. Box. 35856-98613, Islamic Republic of Iran*

Mousa Aliahmad and Fardin Sadeghfari

*Department of Physics, University of Sistan and Baluchestan,  
Zahedan, Iran, P. O. Box. 98155-987, Islamic Republic of Iran*

Mahmoud Hashemzai

*Department of Pharmacodynamics and Toxicology,  
School of Pharmacy, Zabol University of Medical Sciences,  
Zabol, P. O. Box. 98616-63335, Islamic Republic of Iran*

(Received 1 February 2017; Accepted 10 February 2017; Published 3 April 2017)

Magnetite ( $\text{Fe}_3\text{O}_4$ ) nanoparticles, are promising inorganic nanomaterials for future biomedical applications due to their low toxicity and unique magnetic properties. However, the synthesis of these particles can often be expensive, energy intensive, and non-scalable, requiring the addition of surfactants to stabilize the material to control the particle size and avoid agglomeration. We wish to report a simple, green, surfactant-free electrochemical synthesis of these materials using a closed aqueous system at ambient temperature. Particle diameter, between 19 and 33 nm, was controlled by simply modifying the distance between the electrodes. These magnetite nanoparticles were then fully characterized using both spectroscopy and microscopy. Vibrational magnetometry indicates that as the size of the particle decreases, the magnetic hysteretic gap decreases, although for samples below 25 nm no inter-sample difference was observed. To support this experimental data, we carried out a Density Functional Theory (DFT) analysis of magnetite containing more than three iron atoms in the cluster, an essential proposition as magnetite contains three distinct iron species. These calculations were used to support the experimental observations, and closely reproduced both the experimental IR spectrum, and the XRD pattern. *In vitro* cytotoxicity assays showed dose responsive behavior for the nanoparticles, and demonstrated that they are non-toxic at clinically relevant concentrations; below 200  $\mu\text{g}/\text{mL}$  we observed no toxicity in a 48-hour standard assay. This work represents the first DFT based simulation of this detailed magnetite cluster, and demonstrates that this sustainable synthetic method is capable of producing nanomaterials with a physical and biological profile that might make them suitable for biomedical applications. [DOI: 10.1380/ejssnt.2017.31]

**Keywords:** Density functional calculations; Electrochemical methods; Field emission spectroscopy; Iron oxide; Nano-particles, quantum dots, and supra-molecules; Biological aspects of nano-structures;

## I. INTRODUCTION

Academic interest in magnetite ( $\text{Fe}_3\text{O}_4$ ) nanoparticles (iron oxide nanoparticles, IONPs) has grown steadily in recent decades [1–9], not only because of their unique magnetic properties, but also because their low toxicity and overall biocompatibility make them promising materials for various biomedical applications. The proposed uses include targeted drug-delivery, hyperthermic therapy, magnetic resonance imaging, immunoassays, and for biochemical separation science [10–18].

These magnetite IONPs have been prepared using a variety of techniques including sol-gel formation [19, 20], hy-

drothermal approaches [21, 22], solid state synthesis [23–25], wet milling [26, 27], pyrolysis [28, 29], microemulsion [30–32], and electrochemistry [33, 34]. However, although the ease and control of the electrochemical method has made it a particularly promising approach, surfactants are often used to assist in the synthesis and prevent aggregation. Consequently, as it is difficult to completely remove all traces of the surfactant from the IONPs, and as some surfactants have been shown to be cytotoxic [35, 36], we have pursued an additive-free approach for the electrochemical synthesis of these materials as bare nanoparticles. This is also, of course, a more sustainable and green strategy. We wish to report the preliminary results from our new additive-free sustainable procedure for the synthesis of iron-oxide nanoparticles, using inexpensive iron (II) sulfate heptahydrate as the iron source and sodium hydroxide to control the pH of the solution (a full study of the effect of the pH on the synthesis will follow this

\* Corresponding author: j.trant@uwindsor.ca

† Corresponding author: a.rahdar@uoz.ac.ir

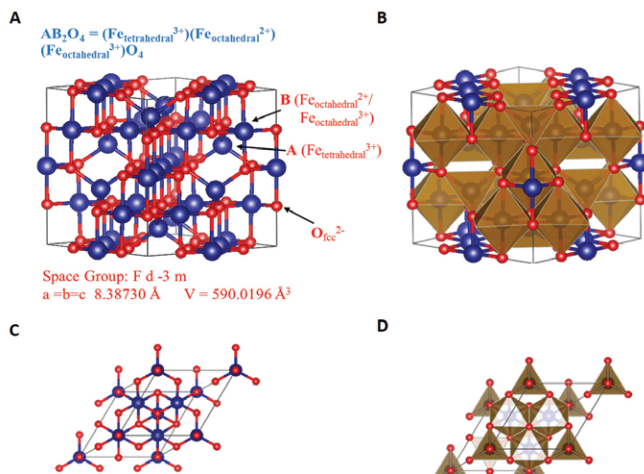


FIG. 1. Schematic view of the inverse spinel crystal structure of magnetite ( $\text{Fe}_3\text{O}_4$ ): A) ball and stick model of the cubic unit cell; B) polyhedral model of the cubic unit cell (Unit-cell volume =  $590.0196 \text{ \AA}^3$ ); C) the rhombohedral primitive cell of  $\text{Fe}_3\text{O}_4$ ; D) three-dimensional model of the rhombohedral primitive cell C, atoms at the apexes of the triangles lie in the same plane.  $\text{Fe}_{\text{oct}} = \text{blue}$ ,  $\text{Fe}_{\text{tet}} = \text{blue}$  and  $\text{O} = \text{red}$ .

publication) as the only reagents.

The synthesis was carried out in a closed water system without the need for inert gas, again reducing the environmental impact of the synthesis. Two steel plates are used as the anode and cathode, and distilled water as the electrolyte. All syntheses occurred under identical alkaline conditions ( $\text{pH}=13$ ) with an initial concentration of iron sulfate (4 g of iron (II) sulfate,  $\text{FeSO}_4$ ) dissolved in 200 ml of the double distilled water and a current density of  $31.4 \text{ mA/cm}^2$ . The only variable needed to tune the size of the particles was the distance between the electrodes. The IONPs were then characterized using X-ray powder diffraction (XRD), Fourier-transform infrared spectroscopy (FT-IR), vibrating sample magnetometry (VSM), and field emission scanning electron microscopy (FESEM). The experimental results were then compared with the theoretical values, and were found to be in general agreement. The cytotoxicity of these IONPs was then evaluated by a 3-(4,5-dimethylthiazol-2-yl)-2,5-diphenyltetrazolium bromide (MTT) assay.

## II. EXPERIMENTAL

### A. Materials and reagents

Iron (II) sulfate heptahydrate ( $\text{FeSO}_4 \cdot 7\text{H}_2\text{O}$ ; Sigma-Aldrich) and sodium hydroxide (Sigma-Aldrich) were analytical grade and were used as received without further purification. DU145, a human adenocarcinoma cell line, was purchased from the Pasteur Institute (Iran).

### B. Synthesis of iron oxide nanoparticles (IONPs)

The magnetite nanoparticles were prepared using a surfactant-free electrochemical approach [37, 38]. The following synthesis was carried out in a closed distilled water system, under ambient atmosphere and temperature. The distance between the anode (stainless steel) and the cathode (stainless steel) was varied between 2 and 6 cm for the different preparations, with a constant current density of  $4.31 \text{ mA} \cdot \text{cm}^{-2}$ . The reaction solution was prepared by dissolving iron sulfate heptahydrate (4 g, 14.4 mmol) in 200 mL of doubly distilled water to provide a 72 mM solution of  $\text{Fe}^{2+}$ . Two steel plates ( $13 \times 23 \times 0.5 \text{ mm}$ ) were then electroplated with the solution at  $130.43 \text{ mA} \cdot \text{cm}^{-2}$  for 3 hours. This created the initial layer of iron oxide [37]. The anode and cathode were then replaced and a solution of sodium hydroxide (1 M, 30 mL) was then added dropwise to bring the pH to the desired level. The electrochemical reaction was then allowed to continue at  $4.31 \text{ mA} \cdot \text{cm}^{-2}$  for 3 hours before the current was removed. The particles deposited on the iron-coated steel plates were then collected, and were also extensively washed with double distilled water through iterative rounds of suspension, vortexing, centrifugation, and decanting. The material was then dried for 2 hours at  $60^\circ\text{C}$ , and stored until analyzed.

### C. Computational methodology

The computational calculations for our proposed iron oxide clusters ( $\text{Fe}_4$  and  $\text{Fe}_5$ ) were performed using the Gaussian 09 suite of programs [39]. Our computational models were generated with Gauss View and optimized using the DFT hybrid B3LYP functional (Becke 3-term correlation functional; Lee, Yang, and Parr exchange function) with the 6-31G(d,p) basis set at 298.15 K ( $25^\circ\text{C}$ ) [40]. All of the optimized clusters were verified by frequency computations as minima (zero imaginary frequencies). From these values we were able to graph the predicted IR spectrum.

To accurately predict the ground state of iron oxide, single point calculations was performed on B3LYP/6-31G(d,p) optimized geometries using the split valence basis sets with inclusion of polarized and diffused effects, 6-311++G(d,p) in both low and high spin states [41, 42]. It is known that DFT is a one of the suitable approaches in modeling iron oxide nanoparticles and is a reliable predictor of energy and the other properties of the molecule [43]. The crystallographic data of the magnetite iron oxide ( $\text{Fe}_3\text{O}_4$ , ICSD 43001) was obtained from the report by Ma and co-workers [44]. The cubic magnetite unit cell of a cluster containing 56 atoms ( $\text{Fe}_{24}\text{O}_{32}$ ) was found to be a sufficient structure to model our synthetic iron oxide nanoparticles (Fig. 1). From this structure, a 3D crystal structure visualization and a theoretical XRD spectrum were generated and simulated using VESTA (Visualization for Electronic and Structural Analysis) [45].

#### D. Characterization of iron oxide nanoparticles

All materials were analyzed using X-ray diffractometry (Bruker D8 Advance diffractometer with a Cu-K $\alpha$  ( $\lambda = 1.54\text{\AA}$ ) radiation source), vibrating magnetometry (Meghnatis Daghigh Kavir Co.; Kashan Kavir; Iran) and field emission scanning electron scanning (Mira 3-XMU; BSE-In beam, SE-In beam). The theoretical X-ray pattern was simulated by VESTA [45] software using a Cu-K $\alpha 1$  ( $\lambda = 1.54\text{\AA}$ ) radiation source.

#### E. MTT assay

Prostate cancer DU145 cells were cultured in the usual fashion as monolayers in DMEM media supplemented with 10% fetal bovine serum. The cytotoxicity of the nanoparticles was evaluated by the MTT assay, a non-radioactive colorimetric method [46]. The DU145 cells ( $1 \times 10^4$  cells/well) were transferred onto 96-well plates and at 24 h post-seeding, different concentrations (i.e. ranging from 12.5 to 200  $\mu\text{M}$ ) of nanoparticles were added to each well. The treated cells were then incubated for either 24, 48, or 72 h. After the indicated times, the media was removed and cells were treated with (3-(4, 5-dimethylthiazol-2-yl)-2, 5-diphenyltetrazolium bromide (MTT). The plates were then incubated for 4 h at 37°C in a CO<sub>2</sub> incubator. Finally, the media was removed and absorbance of formed formazan crystals was read at 570 nm by adding DMSO (200  $\mu\text{L}$ ) and Sorenson's buffer (25  $\mu\text{L}$ ) to each well. The absorbance was assessed at a wavelength of 545 nm using a spectrophotometer (Elisa reader, Biochrom Anthos 2020 microplate reader) and cell viability was calculated according to the standard method [46]. The data for the 48 hour study is provided in this manuscript, the others were left out due to space constraints, but are consistent with the results.

### III. RESULTS AND DISCUSSIONS

The nanoparticles were prepared as described above using a green, organic solvent, carrier gas, and surfactant-free process. Five batches were prepared, the only difference being the spacing between the anode and the cathode (from 2 to 6 cm in one cm increments). During our experiments, we found that the nanoparticles adhered poorly to the steel plates; consequently, to obtain a better surface, the plates were first electroplated with the iron oxide to create a better substrate. This was accomplished by simply using a higher current. Following the creation of the amorphous iron oxide surface, the current was then decreased to control the particle size, and the nanoparticles were selectively formed and deposited with a very small size dispersity. Following synthesis, the nanoparticles were recovered, dried, and stored for our studies. However, before these molecules were characterized, the core crystal structure of magnetite was used to develop a computational model to explore the unique properties of this material.

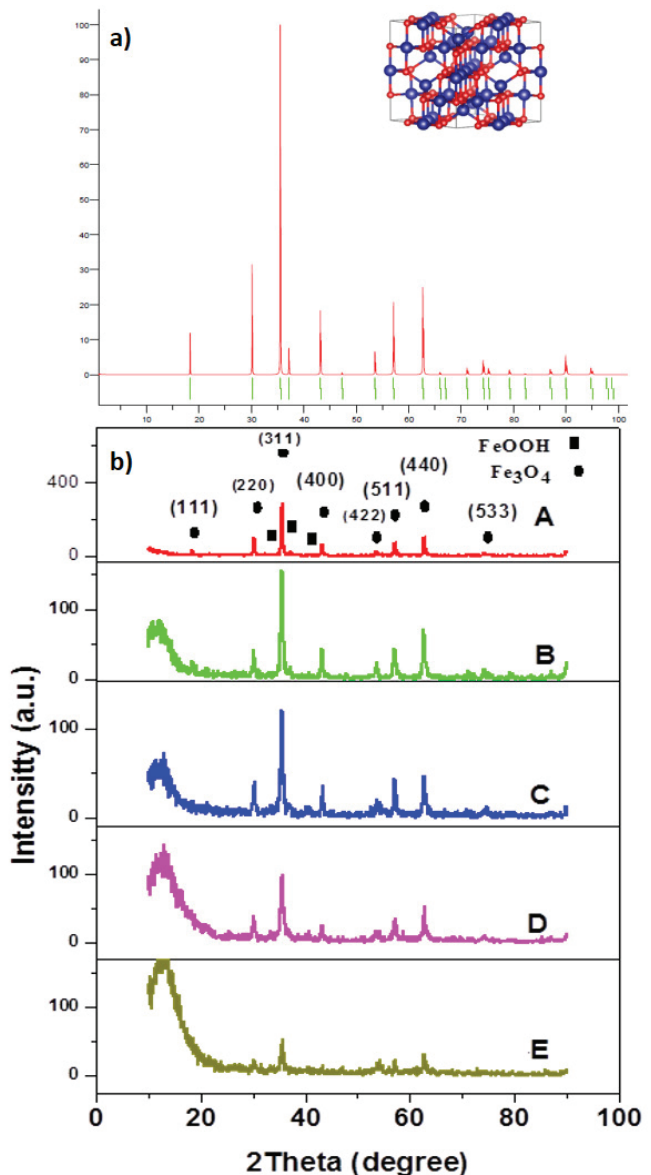


FIG. 2. a) Theoretical XRD simulated by VESTA based on ICSD #43001 [43] and b) experimental XRD patterns of the IONPs as a function of electrode spacing at constant current density ( $4.31 \text{ mA} \cdot \text{cm}^{-2}$ ).

#### A. Magnetite ( $\text{Fe}_3\text{O}_4$ ) structure determination and computational study

$\text{Fe}_3\text{O}_4$  is a metal oxide that crystallizes in a spinel face-centered cubic unit cell structure with the general formula  $\text{AB}_2\text{O}_4$ , where A and B represent different oxidation states of the same cation. This can be better represented as  $(\text{Fe}^{3+}_{\text{tetrahedral}})(\text{Fe}^{2+}_{\text{octahedral}})(\text{Fe}^{3+}_{\text{octahedral}})\text{O}_4$ . As shown in Fig. 1, FeA sites correspond to eight ferric ions at tetrahedral sites where each of them has four oxide ions nearest neighbors; FeB sites correspond to eight ferric ions and eight ferrous ions at octahedral sites each with six oxygen ions. This spinel structure is based on an fcc arrangement of the  $\text{O}^{2-}$  anion lattice, where 1/8 of the tetrahedral sites and 1/2 of the octahedral spaces are occupied. In a cubic inverse spinel iron oxide structure of this class, all of the

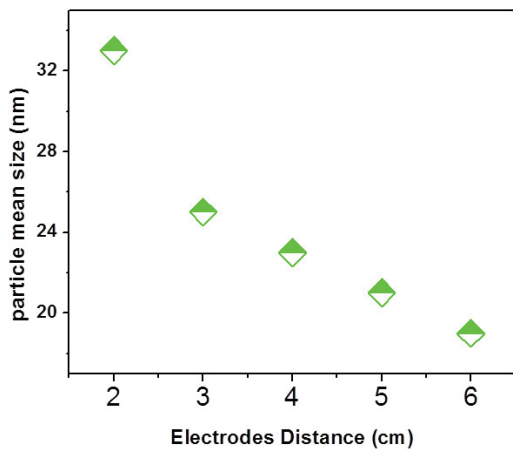


FIG. 3. Mean IONP diameter, as determined by application of the Scherer formula to the XRDs in Fig. 2, as a function of the distance between the electrodes.

$\text{Fe}^{2+}$  ions reside in half of the octahedral sites while the  $\text{Fe}^{3+}$  occupy the balance of the octahedral sites and all of the tetrahedral sites [47, 48]. The simultaneous presence of both  $\text{Fe}^{2+}$  and  $\text{Fe}^{3+}$  in the octahedral sites results in a variety of interesting properties [47, 49–51]. Visual representations of the models used for the crystal structure of the bulk magnetite ( $\text{Fe}_3\text{O}_4$ ) unit cell and the primitive unit cell are provided in Fig. 1 (as ball and stick and polyhedral models to highlight the tetrahedral and octahedral sites). This mixed valence nature makes the bulk structure of these materials challenging to model computationally, and this has limited their theoretical examination, compared with other simpler iron oxide isoforms [52].

Figure 2 shows the XRD diffraction pattern of our synthesized nanomagnetite as a function of electrode distance (Fig. 2b). The expected Bragg peaks for  $\text{Fe}_3\text{O}_4$  were obtained at the  $2\theta$  values of  $18.4^\circ(111)$ ,  $30.5^\circ(220)$ ,  $35.9^\circ(311)$ ,  $37^\circ(222)$ ,  $43.5^\circ(400)$ ,  $47.6^\circ(422)$ ,  $57.3^\circ(511)$ ,  $63.1^\circ(440)$  and  $74.1^\circ(533)$ . Another iron-containing species (indicated by the filled square) was also observed with Bragg peaks at  $2\theta$  values of  $33.4^\circ(400)$  and  $39.5^\circ(301)$ . These spectra correlate well with the simulated theoretical diffraction of magnetite calculated from a published crystal structure ( $\text{Fe}_3\text{O}_4$ , ICSD Collection Code 43001, Fig. 2a) [44]. They are also in agreement with the calculated XRD from other deposited crystal structures of magnetite ( $\text{Fe}_3\text{O}_4$ , ICSD Collection Code 82237, data not shown) [53].

Nanoparticles were synthesized using five different spacings between the electrodes: 2, 3, 4, 5, and 6 cm, to provide the five differing IONP preparations: **A**, **B**, **C**, **D** and **E** respectively. The standard Bragg peaks corresponding to  $\text{FeOOH}$  and  $\text{Fe}_3\text{O}_4$  are identified in the 2 cm spectrum (Fig. 2b, **A**). Note that the signal/noise ratio improves as the electrode gap becomes smaller.

As is apparent in Fig. 2, the degree of crystallinity of the IONPs increases as the distance between the electrodes decreases (i.e. **A** clearly appears more crystalline than **C**); nanomagnetite crystallinity is inversely proportional to electrode spacing. This effect most likely arises because with a shorter distance, the nascent IONPs forming at the anode do so in the presence of a higher con-

centration of hydroxide (in the case of a shorter electrode spacing), which directly leads to increased levels of crystallinity. Similarly, as the distance increases, the rate of reaction decreases, as is evidenced by the smaller particle sizes formed at the longer distances [37]. The relative abundance of this material appears to increase steadily as the electrode spacing increases from 2 through 6 cm. The average crystallite size ( $D$ ) of the IONPs was calculated quantitatively by the Scherer formula (Equation 1) using the strongest plane reflection from the XRD pattern (3 1 1) [54–57]:

$$D_{h,k,l} = \frac{K\lambda}{\beta_{h,k,l} \cos \theta}, \quad (1)$$

where  $\lambda$  is the X-ray wavelength ( $\lambda = 1.542 \text{ \AA}$ ;  $\text{CuK}\alpha$ ),  $K$  is a constant related to the particle shape ( $K = 0.9$  for spherical particle),  $\beta$  is the full width at half maximum (FWHM) of the line, and  $\theta$  is the diffraction angle.

The impurities in our synthesized sample could be due to the presence of surface hydroxyl groups, the most common impurity observed on a freshly prepared  $\text{Fe}_3\text{O}_4$  surface. In bulk formulations, this surface functionalization is negligible as a percentage of the iron atoms, but it becomes far more relevant in these types of nanoformulations where the surface area/volume ratio is very high [58, 59]. The effect of this impurity on the structure and electronic properties of the magnetite surface was studied in detail by Parkinson and co-workers using photoemission spectroscopies, scanning tunneling microscopy, and density-functional theory [60]. They report that the surface absorption of hydroxide led to the significant change in structural and electronic properties of iron oxide surface via a semiconductor-half metal transition process. A second possible explanation for these peaks could be due to the adsorption of water on  $\text{Fe}_3\text{O}_4$  surface. However, this class of material has been investigated both experimentally and computationally on several occasions [61–63]. Iron oxide magnetite nanoparticles tend to be oxidized in air to generate maghemite ( $\gamma\text{-Fe}_2\text{O}_3$ ) and/or hematite ( $\alpha\text{-Fe}_2\text{O}_3$ ) depending on the incubation temperature. The peaks associated with maghemite and hematite [(113), (210); and (213), (210), respectively] [64, 65] are not present in our XRD spectra indicating that our synthesized magnetite has not degraded according to these oxidation pathways. However, this impurity could be a different highly oxidized form of iron oxide arising from the electrochemical synthesis.

Our XRD spectra are partially consistent with the presence of  $\gamma\text{-FeOOH}$  and/or surface hydroxyl groups. Specifically, the  $\gamma\text{-FeOOH}$  material has been previously assigned in the reported XRD pattern of a complex  $\text{Fe}_3\text{O}_4/\text{Fe}_2\text{O}_3/\text{FeCO}_3/\text{FeOOH}$  material [66]. The indicated low intensity diffraction signals of our synthetic nanoparticle are consistent with lepidocrocite,  $\gamma\text{-FeOOH}$ , a polymorphous modification of iron hydroxide [67]. However, from this data alone, it is impossible to determine whether this isoform is only localized to the surface, or is present throughout the internal crystal structure of the nanoparticles. This distinction is important as differing internal geometries play an important role [48, 60] in determining the behavior of magnetite-based electronic and spintronic devices. Surface alone vs internal oxidation would also have significant implications for their

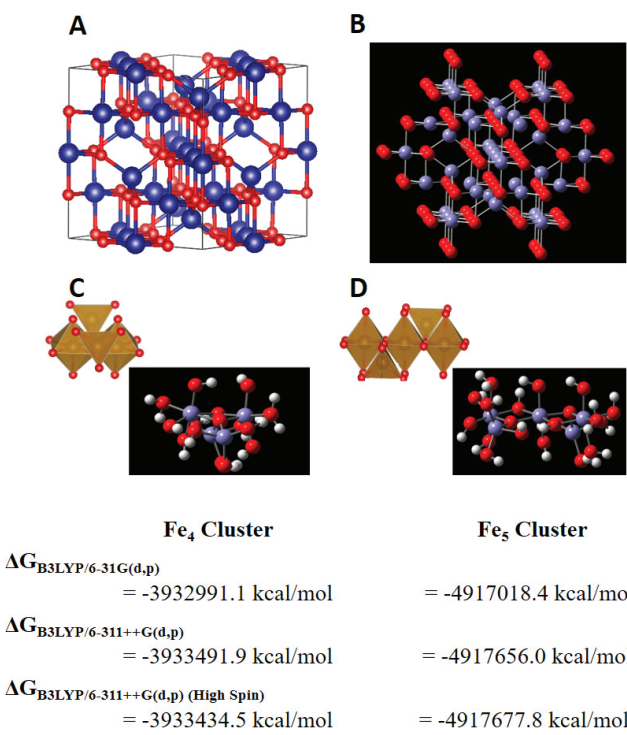


FIG. 4. A) Crystal structure of magnetite [43]. B) Computational model generated based on the crystal structure. C) Four iron atom cluster ( $\text{Fe}_4$ ) derived from cutting the model. D) Alternative cut of the model to obtain a five iron atom cluster ( $\text{Fe}_5$ ). The clusters presented in C and D have been optimized using the B3LYP/6-31G(d,p) level of theory. The optimized and single point energies obtained from these structures at different levels of theory is provided below the figure. Blue represents Fe, Red represents O, white represents H.

biomedical application [68], thus a detailed understanding of the presence of different defects in the magnetite (i.e. surface defects and impurities as well as bulk defects) is required [69]. Most of the reported theoretical studies of iron oxides focused on mononuclear and binuclear forms [70–74]. To the best of our knowledge, this is the first DFT study of a magnetite cluster with more than three atoms [75], as we are taking into account the non-equivalent populations of the different iron atoms. This is somewhat surprising as there are three distinct iron atoms ( $\text{Fe}_{\text{oct}}^{2+}$ ,  $\text{Fe}_{\text{tet}}^{3+}$ , and  $\text{Fe}_{\text{oct}}^{3+}$ ) present in the mineral in non-equal proportions.

To investigate this complex system, and to attempt to determine the nature of the observed impurities, we prepared two cluster models containing either an even ( $\text{Fe}_4$ ) or odd ( $\text{Fe}_5$ ) number of iron atoms (Fig. 4). These structures were derived from the (001) slab surface model presented in Fig. 1A. In both clusters, the terminal groups were saturated with hydrogens (making the exposed oxides hydroxides) to ensure an overall neutral. As shown in Fig. 4, in cluster  $\text{Fe}_4$ , two  $\text{Fe}_{\text{oct}}$  are coordinated by  $\mu_3$ -oxo (an oxide ion bound to three irons: two  $\text{Fe}_{\text{oct}}$  and one  $\text{Fe}_{\text{tet}}$ ); while in cluster  $\text{Fe}_5$ , two  $\text{Fe}_{\text{oct}}$  are coordinated by both a  $\mu$ -hydroxo (a hydroxide ion bound to two  $\text{Fe}_{\text{oct}}$ ) and a  $\mu_3$ -oxo (an oxide ion bound to three irons: two  $\text{Fe}_{\text{oct}}$  and one  $\text{Fe}_{\text{tet}}$ ). In the optimized  $\text{Fe}_4$  structure, the cal-

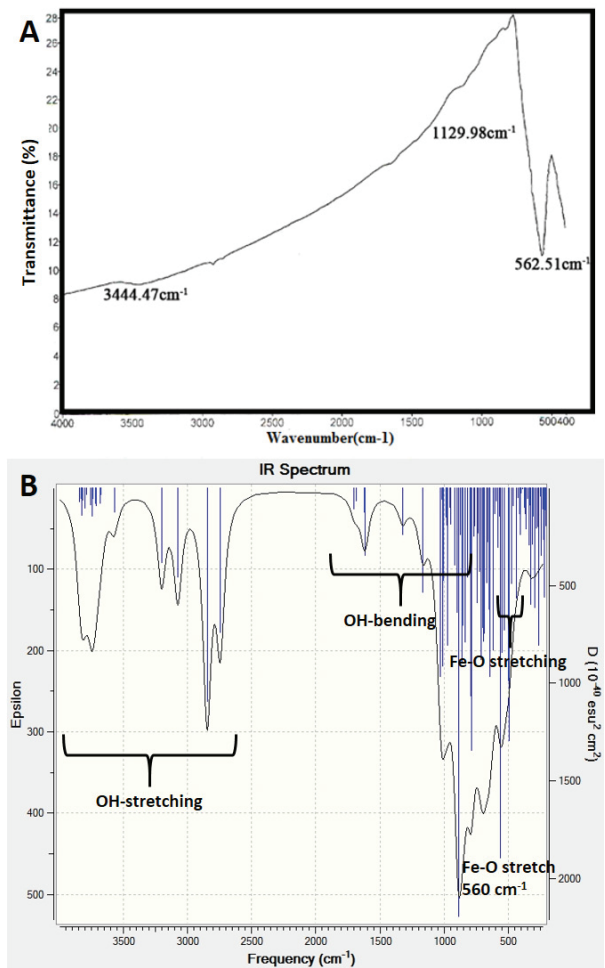


FIG. 5. A) Uncorrected FT-IR spectrum of magnetite nanoparticles. Scans were carried out from 4000 to 400  $\text{cm}^{-1}$  and the data was obtained at ambient temperature and atmosphere from a KBr pellet. B) Predicted FT-IR spectrum calculated from the  $\text{Fe}_5$  cluster (blue lines are the calculated values (tabulated in the Supplementary materials as Table S1), the black outline is the linear combination of these values). The vibration signals are labelled, note that due to the small size of the cluster, a large number of hydroxyl groups are present. This results in the strong O-H stretches at high wave numbers that are not present or expected in the experimental spectrum.

culated mean values of  $\text{Fe}_{\text{oct}}-\text{Fe}_{\text{oct}}$  and  $\text{Fe}_{\text{oct}}-\text{Oeq}$  bond lengths were found to be 2.92 and 1.90 Å, respectively. Small differences between these three types of inter atomic distances are predicted for  $\text{Fe}_5$ . In this larger size cluster, the average  $\text{Fe}_{\text{oct}}-\text{Fe}_{\text{oct}}$  and  $\text{Fe}_{\text{oct}}-\text{O}_{\text{eq}}$  bond lengths were found to be 2.94 and 1.91 Å, respectively. This is a match with the reported bond distances in the bulk magnetite (2.96 and 2.06 respectively) [67–69]. The difference in Fe–O bond length is mostly attributable to the Fe–O–H functions in our cluster rather than the Fe–O–Fe bonds observed in the bulk structure.  $\text{Fe}_5$  may well act as a suitable minimum model of the mixed valence nature of magnetite, to allow for an initial investigation into the properties of nanomagnetite. A series of single point calculations at higher levels of theory on both the low- and high-spin states on the B3LYP/6-31G(d,p) optimized geometries were also performed. As expected, the energetic

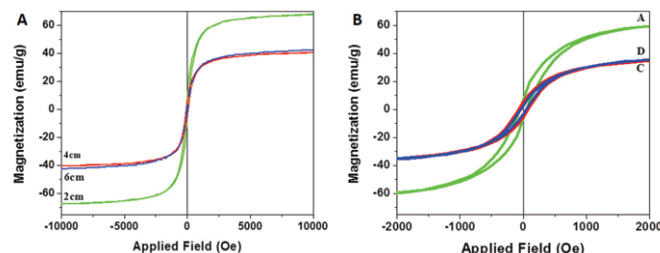


FIG. 6. VSM derived magnetization plots of the IONPs; A) Full spectrum, B) expansion to clearly show the hysteresis loop.

TABLE I. Magnetic parameters of the nanomagnetite formulations.

sample	Particle diameter (nm)	(Magnetic Remanence) M <sub>r</sub>	H <sub>c</sub> (Oe)	(Magnetic saturation) M <sub>s</sub>
A	33	5.98	100	68
C	23	5.75	100	40.5
E	19	2.97	0	42.4

estimation improves at higher levels of theory for both low and high spin state magnetite. Coordinates and thermochemical data of all optimized clusters, and their related single point energies are provided in the supplementary materials.

Ongoing efforts are focused on the application of quantum mechanical calculations based on advanced density functional theory (DFT) modelling of mixed clusters with a larger number of iron atoms with different multiplicities, as properties of the clusters depend on the multiplicity of their electronic state ( $M = 3, 5, 7, 9, 11, 13, 15$ , and  $17$ ). We are also currently evaluating the interaction between the magnetite surface and different impurities to better match our experimental XRD spectrum and to better define the structural and electronic nature of this class of nanoparticle for compatibility with potential biomedical applications. These results will be published in due course.

The FT-IR transmission spectra of the IONP prepared at 2 cm (sample A) taken on a JASCO 640 plus infrared spectrometer is provided as Fig. 5A. The FT-IR samples were prepared by mixing the IONP powder with KBr. This material was then pressed and ground into a transparent pellet with a diameter of 1 cm in the usual fashion.

The nature of the IONPs were further confirmed by this analysis. As seen in the spectrum, there is a broad absorption centered at  $3444\text{ cm}^{-1}$  consistent with an O–H stretching vibration from absorbed water or surface functionalization from the presence of Fe–O–H or Fe–O–O–H impurities. The bending mode for this same functionality is observed at  $1590\text{ cm}^{-1}$ . The only other major peak observed is at  $562\text{ nm}$ , which is in the typical range observed for the Fe–O stretch in magnetite derived

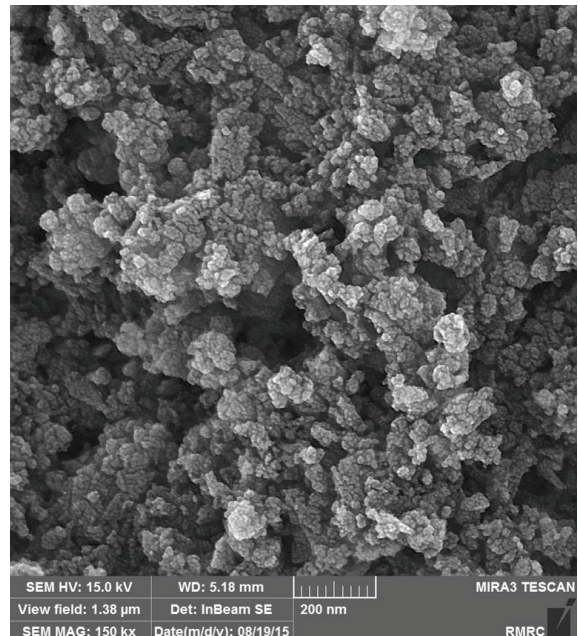


FIG. 7. The FESEM of the magnetite nanoparticles (sample E). The scale bar represents 200 nm, and the field of view is approximately  $1.38\text{ }\mu\text{m}$ . The particles appear quasi-spherical with a mean particle size of about 20.5 nm (determined by Image J software). The mean crystal size estimated from the specific surface XRD above is about 19 nm, which agrees with that measured by FESEM.

nanoparticles, although it is lower than previously observed ( $570\text{--}590\text{ cm}^{-1}$ ) [79–81]. However, the power of this surfactant-free technique is evidenced by the lack of organic components in the FT-IR; even in the well cleaned particles synthesized through other routes, significant organic IR impurities are inevitably present [82, 83]. This is normally necessary to functionalize the surface of the particles for stabilization. An FT-IR spectrum was also calculated based on our  $\text{Fe}_5$  cluster (Fig. 5B, spectrum is tabulated as Table S1 in the Supplementary materials). As this cluster has a very high surface to volume ratio, the Fe–O–H stretches are very apparent compared to the experimental spectrum. However, of significant note is the close correlation of the strongest Fe–O stretch, observed at  $560\text{ cm}^{-1}$  with the observed experimental maximum at  $562\text{ cm}^{-1}$ . It is also of note that the different stretches attributable to the different Fe–O bonds present in magnetite, ( $450\text{--}590\text{ cm}^{-1}$ ), might explain the significant line broadening in that region of the experimental spectrum. Peaks above this value are attributed to the O–H bending modes present in our cluster. This FT-IR data, in conjunction with the XRD results suggest that in the current case, the surface of the particles is functionalized with –OH and/or O–O–H functionalities rather than through organic capping and coating.

Vibrating sample magnetometry (VSM) was then used to determine if the magnetic properties varied with particle diameter (Fig. 6). The presence of a hysteresis loop (clearly seen in the expansion, Fig. 6b) indicates that the IONPs possess ferromagnetic properties. This was expected, as it has usually been observed for ferromagnetic materials with diameters larger than 10 nm [37]. The

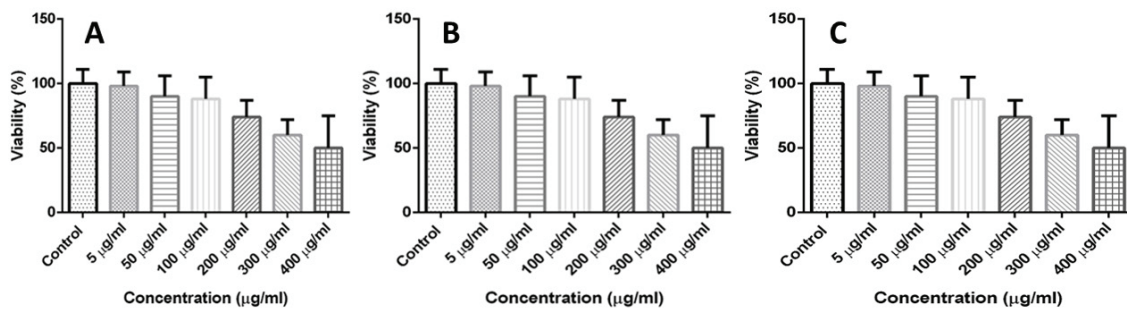


FIG. 8. MTT assay results from cells following a 48 hour incubation with IONPs. A) MTT assay of sample A (33 nm); B) MTT assay of sample C (23 nm); C) MTT assay of sample E (19 nm).

amplitude of this hysteresis loop has been attributed to the magnetic anisotropy of the crystalline lattice and is influenced by the presence of impurities within the materials [37, 54–56]. Our IONPs show the expected low saturation magnetization ( $M_s$ ) values compared to those of the  $\text{Fe}_3\text{O}_4$  bulk materials (~85–100 emu/g) [38, 57, 84, 85]; consequently, these IONPs may form a suitable platform for developing magnetic resonance imaging (MRI), cell separation and medical diagnostic applications. The lower  $M_s$  value of nanoformulated  $\text{Fe}_3\text{O}_4$  compared to the bulk material has been attributed to the extremely high surface area/volume ratio and cation distribution [38, 85]. As apparent from Fig. 6 and Table I, the saturation magnetization of the magnetic nanoparticles follows an interesting non-linear pattern. The largest particles (A, 33 nm) have a considerably higher  $M_s$  than the smaller particles. However, despite the difference in size between the other two samples (23 and 19 nm) there is no significant difference in  $M_s$ . However, the coercivities between the latter two samples do differ, but are either 0 or 100, intermediate values are not observed for these nanomaterials. This is attributed to the randomly oriented, uniaxial and non-interacting behavior of IONPs [37].

Field emission scanning electron microscopy (FESEM) image of IONP E is shown in Fig. 7 (Field of view is approximately 1.5  $\mu\text{m}$ ). This FESEM data, suggesting a particle size of 20.5 nm, is in close agreement with our XRD data, and supports the conclusion that the size of the particles can be tuned by simply changing the distance between the electrodes during their synthesis.

Following this physical characterization, the materials were evaluated for biocompatibility through an MTT assay. As noted, the surface of our materials is possibly functionalized with hydroxide or hydroperoxide moieties, and if so, this might have a detrimental effect on cells. The results of the 48 hour incubation MTT assay study of the IONPs are shown in Fig. 8. As much lower toxicity profiles were found for the shorter incubation times (data not shown), this longer assay was deemed necessary to determine the dose-dependent toxicity of these materials.

As shown in Fig. 8, the IONPs demonstrate no significant toxicity at the lower concentrations, however, above 200  $\mu\text{g}/\text{mL}$ , mean cell viability drops below 70% for all three formulations suggesting toxic effects become significant at this dose [86]. This is in contrast to other reports on IONP toxicity, where concentrations as low as 15  $\mu\text{g}/\text{mL}$  were shown to result in significant toxic-

ity [87, 88]. The exact mechanism of toxicity, and possible explanations for the differential response to our formulation, will be examined in our following full report. 200  $\mu\text{g}/\text{mL}$  is, however, a relatively high concentration indicating that the IONPs are reasonably well tolerated by the DU145 cells. Cytotoxicity also appears to be independent of particle size.

#### IV. CONCLUSIONS

IONPs of  $\text{Fe}_3\text{O}_4$  with nearly spherical shapes and mean diameters ranging from 19 to 33 nm were synthesized through our novel, sustainable, surfactant-free electrochemical method in an alkaline aqueous system. No inert carrier gas was required, and the synthesis was carried out in a closed water loop, greatly reducing waste, and making this a very inexpensive approach to the synthesis of these materials. Nanoparticle formation was confirmed by XRD analysis. In addition, the X-Ray diffraction pattern also indicated that there were some impurities in the form of  $\text{FeOOH}$  or  $\text{FeOH}$ , which was supported by the FT-IR data. Our computational modelling, including the cluster models of magnetite containing four or five iron atoms, provided bond lengths similar to those observed in the crystal structure and also provided an FT-IR spectrum that matched the experimental values. The five-iron atom cluster model ( $\text{Fe}_5$ ) proved to be a good minimum model for our preliminary investigations into the theoretical behavior of the bulk structure of magnetite. The ferro-magnetic and superparamagnetic behavior of the IONPs was characterized using VSM. Our results indicated that IONP size was inversely proportional to the distance between the electrodes used during the synthesis. In addition, the magnetic saturation and remanence decreased as the distance between electrodes decreased. Despite their possibly reactive surface functionalization, the IONPs proved to be biocompatible with the DU145 cells line at moderate concentrations, and the observed cytotoxicity appears to be independent of the particle size or crystallinity. Further details on the synthesis and biological behavior, including antibiotic and mammalian *in vivo* studies will be published in a full paper. The exhibited properties, and moderate toxicity makes this class of IONPs potential candidates for future biomedical applications.

## ACKNOWLEDGMENTS

S.M.T and J.F.T would like to thank the University of Windsor for providing funding for this project. This work was made possible by the facilities of the Shared Hierarchical Academic Research Computing Network (SHARCNET:www.sharcnet.ca) and Compute/Calcul Canada. M.A. and F.S. would like to thank the University of Sistan and Baluchestan for financial support for this work.

The authors declare that they have no competing financial interest.

## APPENDIX

DFT calculated geometries, thermochemical data, and the related single point energies, and Calculated IR spectrum data of Fe<sub>5</sub> iron oxide cluster are available in Supplementary materials ([https://www.jstage.jst.go.jp/article/ejssnt/15/0/15\\_31/\\_article/supplement](https://www.jstage.jst.go.jp/article/ejssnt/15/0/15_31/_article/supplement)).

- 
- [1] S. Laurent, D. Forge, M. Port, A. Roch, C. Robic, L. V. Elst, and R. N. Muller, *Chem. Rev.* **108**, 2064 (2008).
- [2] W. Wu, C. Z. Jiang, and V. A. L. Roy, *Nanoscale* **8**, 19421 (2016).
- [3] F. Assa, H. Jafarizadeh-Malmiri, H. Ajamein, N. Anarjan, H. Vaghari, Z. Sayyar, and A. Berenjian, *Nano Res.* **9**, 2203 (2016).
- [4] N. M. Dissanayake, K. M. Current, and S. O. Obare, *Int. J. Mol. Sci.* **16**, 23482 (2015).
- [5] M. B. Gawande, P. S. Branco, and R. S. Varma, *Chem. Soc. Rev.* **42**, 3371 (2013).
- [6] G. Liu, J. Gao, H. Ai, and X. Chen, *Small* **9**, 1533 (2013).
- [7] D. Ling and T. Hyeon, *Small* **9**, 1450 (2013).
- [8] S. Laurent, A. A. Saei, S. Behzadi, A. Panahifar, and M. Mahmoudi, *Expert Opin. Drug Delivery* **11**, 1449 (2014).
- [9] P. B. Santhosh and N. P. Ulrich, *Cancer Lett.* **336**, 8 (2013).
- [10] S. J. H. Soenen, U. Himmelreich, N. Nuytten, and M. De Cuyper, *Biomaterials* **32**, 195 (2011).
- [11] T.-Y. Liu, S.-H. Hu, D.-M. Liu, S.-Y. Chen, and I. W. Chen, *Nano Today* **4**, 52 (2009).
- [12] B. Gaihre, M. S. Khil, D. R. Lee, and H. Y. Kim, *Int. J. Pharm.* **365**, 180 (2009).
- [13] X. Jia, L. Tan, Y. Zhou, X. Jiang, Q. Xie, H. Tang, and S. Yao, *Electrochim. Commun.* **11**, 141 (2009).
- [14] S. Murakami, T. Hosono, B. Jeyadevan, M. Kamitakahara, and K. Ioku, *J. Ceram. Soc. Jpn.* **116**, 950 (2008).
- [15] R. Hiergeist, W. Andrä, N. Buske, R. Hergt, I. Hilger, U. Richter, and W. Kaiser, *J. Magn. Magn. Mater.* **201**, 420 (1999).
- [16] T. Hartikainen, J.-P. Nikkanen, and R. Mikkonen, *IEEE Trans. Appl. Supercond.* **15**, 2336 (2005).
- [17] R. Melamed and A. B. da Luz, *Sci. Total Environ.* **368**, 403 (2006).
- [18] K. M. Pang, S. Ng, W. K. Chung, and P. K. Wong, *Water, Air, Soil Pollut.* **183**, 355 (2007).
- [19] N. J. Tang, W. Zhong, H. Y. Jiang, X. L. Wu, W. Liu, and Y. W. Du, *J. Magn. Magn. Mater.* **282**, 92 (2004).
- [20] J. Xu, H. Yang, W. Fu, K. Du, Y. Sui, J. Chen, Y. Zeng, M. Li, and G. Zou, *J. Magn. Magn. Mater.* **309**, 307 (2007).
- [21] T. J. Daou, G. Pourroy, S. Bégin-Colin, J. M. Grenèche, C. Ulhaq-Bouillet, P. Legaré, P. Bernhardt, C. Leuvrey, and G. Rogez, *Chem. Mater.* **18**, 4399 (2006).
- [22] S. Ni, X. Wang, G. Zhou, F. Yang, J. Wang, Q. Wang, and D. He, *Mater. Lett.* **63**, 2701 (2009).
- [23] D. L. Paiva, A. L. Andrade, M. C. Pereira, J. D. Fabris, R. Z. Domingues, and M. E. Alvarenga, *Hyperfine Interact.* **232**, 19 (2015).
- [24] O. Schneeweiss, R. Zboril, N. Pizurova, M. Mashlan, E. Petrovsky, and J. Tucek, *Nanotechnology* **17**, 607 (2006).
- [25] H. Karami, *J. Cluster Sci.* **21**, 11 (2010).
- [26] M. M. Can, S. Ozcan, A. Ceylan, and T. Firat, *Mater. Sci. Eng. B* **172**, 72 (2010).
- [27] D. Chen, S. Ni, and Z. Chen, *China Particulol.* **5**, 357 (2007).
- [28] W. W. Yu, J. C. Falkner, C. T. Yavuz, and V. L. Colvin, *Chem. Commun.*, 2306 (2004).
- [29] W. S. Chiu, S. Radiman, M. H. Abdullah, P. S. Khiew, N. M. Huang, and R. Abd-Shukor, *Mater. Chem. Phys.* **106**, 231 (2007).
- [30] L. P. Ramírez and K. Landfester, *Macromol. Chem. Phys.* **204**, 22 (2003).
- [31] K. M. Lee, C. M. Sorensen, K. J. Klabunde, and G. C. Hadjipanayis, *IEEE Trans. Magn.* **28**, 3180 (1992).
- [32] A. B. Chin and I. I. Yaacob, *J. Mater. Process. Technol.* **191**, 235 (2007).
- [33] L. Cabrera, S. Gutierrez, N. Menendez, M. P. Morales, and P. Herrasti, *Electrochim. Acta* **53**, 3436 (2008).
- [34] D. Ramimoghadam, S. Bagheri, and S. B. A. Hamid, *J. Magn. Magn. Mater.* **368**, 207 (2014).
- [35] W. Wu, Q. He, and C. Jiang, *Nanoscale Res. Lett.* **3**, 397 (2008).
- [36] S. I. Park, J. H. Lim, J. H. Kim, H. I. Yun, J. S. Roh, C. G. Kim, and C. O. Kim, *Phys. Status Solidi B* **241**, 1662 (2004).
- [37] F. Fajaroh, H. Setyawan, W. Widiyastuti, and S. Winardi, *Adv. Powder Technol.* **23**, 328 (2012).
- [38] M. Aliahmad, A. Rahdar, F. Sadeghfar, S. Bagheri, and M. R. Hajinezhad, *Nanomed. Res. J.* **1**, 39 (2016).
- [39] M. J. Frisch, G. W. Trucks, H. B. Schlegel, G. E. Scuseria, M. A. Robb, J. R. Cheeseman, G. Scalmani, V. Barone, B. Mennucci, G. A. Petersson, H. Nakatsuji, M. Caricato, X. Li, H. P. Hratchian, A. F. Izmaylov, J. Bloino, G. Zheng, J. L. Sonnenberg, M. Hada, M. Ehara, K. Toyota, R. Fukuda, J. Hasegawa, M. Ishida, T. Nakajima, Y. Honda, O. Kitao, H. Nakai, T. Vreven, J. A. Montgomery, Jr., J. E. Peralta, F. Ogliaro, M. Bearpark, J. J. Heyd, E. Brothers, K. N. Kudin, V. N. Staroverov, R. Kobayashi, J. Normand, K. Raghavachari, A. Rendell, J. C. Burant, S. S. Iyengar, J. Tomasi, M. Cossi, N. Rega, J. M. Millam, M. Klene, J. E. Knox, J. B. Cross, V. Bakken, C. Adamo, J. Jaramillo, R. Gomperts, R. E. Stratmann, O. Yazyev, A. J. Austin, R. Cammi, C. Pomelli, J. W. Ochterski, R. L. Martin, K. Morokuma, V. G. Zakrzewski, G. A. Voth, P. Salvador, J. J. Dannenberg, S. Dapprich, A. D. Daniels, Ö. Farkas, J. B. Foresman, J. V. Ortiz, J. Cioslowski, and D. J. Fox, *Gaussian 09*, (Gaussian, Inc., Wallingford CT, 2009).
- [40] A. D. Becke, *J. Chem. Phys.* **98**, 1372 (1993).
- [41] J. P. Perdew, K. Burke, and M. Ernzerhof, *Phys. Rev. Lett.* **77**, 3865 (1996).
- [42] J. P. Perdew, K. Burke, and M. Ernzerhof, *Phys. Rev. Lett.* **78**, 1396 (1997).

- [43] E. G. Lewars, in *Computational Chemistry: Introduction to the Theory and Applications of Molecular and Quantum Mechanics* (Springer Netherlands, Dordrecht, 2011), p. 445.
- [44] X. Ma, Z. Zhang, and A. Wang, *Construct. Build. Mater.* **104**, 25 (2016).
- [45] K. Momma and F. Izumi, *J. Appl. Crystallogr.* **44**, 1272 (2011).
- [46] D. T. Vistica, P. Skehan, D. Scudiero, A. Monks, A. Pittman, and M. R. Boyd, *Cancer Res.* **51**, 2515 (1991).
- [47] K. E. Sickafus, J. M. Wills, and N. W. Grimes, *J. Am. Ceram. Soc.* **82**, 3279 (1999).
- [48] J. Noh, O. I. Osman, S. G. Aziz, P. Winget, and J.-L. Brédas, *Chem. Mater.* **27**, 5856 (2015).
- [49] A. Yanase and N. Hamada, *J. Phys. Soc. Jpn.* **68**, 1607 (1999).
- [50] Z. Zhang and S. Satpathy, *Phys. Rev. B* **44**, 13319 (1991).
- [51] D. Santos-Carballal, A. Roldan, R. Grau-Crespo, and N. H. de Leeuw, *Phys. Chem. Chem. Phys.* **16**, 21082 (2014).
- [52] J. Yue, X. Jiang, Y. V. Kaneti, and A. Yu, in *Experimental and theoretical study of low-dimensional iron oxide nanostructures* pp.119, (InTech, 2012).
- [53] A. F. M. Santos, L. J. A. Macedo, M. H. Chaves, M. Espinoza-Castaneda, A. Merkoci, F. d. C. A. Lima, and W. Cantanhede, *J. Braz. Chem. Soc.* **27**, 727 (2016).
- [54] A. Rahdar, M. Aliahmad, and H. Asnaashari, *Adv. Sci. Lett.* **19**, 547 (2013).
- [55] A. Rahdar, M. Aliahmad, and Y. Azizi, *J. Nanostruct.* **5**, 145 (2015).
- [56] Q. A. Pankhurst, J. Connolly, S. K. Jones, and J. Dobson, *J. Phys. D: Appl. Phys.* **36**, R167 (2003).
- [57] R. M. Cornell and U. Schwertmann, in *The Iron Oxides: Structure, Properties, Reactions, Occurrences and Uses*, 2nd Ed. (Wiley-VCH, Weinheim, 2003), p. 139.
- [58] H. Kachkachi, A. Ezzir, M. Noguès, and E. Tronc, *Eur. Phys. J. B* **14**, 681 (2000).
- [59] R. Narayanan and M. A. El-Sayed, *J. Phys. Chem. B* **109**, 12663 (2005).
- [60] G. S. Parkinson, N. Mulakaluri, Y. Losovyj, P. Jacobson, R. Pentcheva, and U. Diebold, *Phys. Rev. B* **82**, 125413 (2010).
- [61] X. Li and J. Paier, *J. Phys. Chem. C* **120**, 1056 (2016).
- [62] G. S. Parkinson, Z. Novotný, P. Jacobson, M. Schmid, and U. Diebold, *J. Am. Chem. Soc.* **133**, 12650 (2011).
- [63] N. Mulakaluri, R. Pentcheva, and M. Scheffler, *J. Phys. Chem. C* **114**, 11148 (2010).
- [64] J. R. Correa, D. Canetti, R. Castillo, J. C. Llópiz, and J. Dufour, *Mater. Res. Bull.* **41**, 703 (2006).
- [65] J. Mürbe, A. Rechtenbach, and J. Töpfer, *Mater. Chem. Phys.* **110**, 426 (2008).
- [66] S. Lian, E. Wang, Z. Kang, Y. Bai, L. Gao, M. Jiang, C. Hu, and L. Xu, *Solid State Commun.* **129**, 485 (2004).
- [67] M. Shopska, Z. Cherkezova-Zheleva, D. Paneva, M. Iliev, G. Kadinov, I. Mitov, and V. Groudeva, *Cent. Eur. J. Chem.* **11**, 215 (2013).
- [68] J. B. Mamani, L. F. Gamarra, and G. E. d. S. Brito, *Mater. Res.* **17**, 542 (2014).
- [69] G. S. Parkinson, *Surf. Sci. Rep.* **71**, 272 (2016).
- [70] J. N. Harvey, in *Principles and Applications of Density Functional Theory in Inorganic Chemistry I*, Eds. N. Kaltsoyanis and J. E. McGrady, (Springer, Berlin, Heidelberg, 2004), p. 151.
- [71] L. Noodleman, *J. Chem. Phys.* **74**, 5737 (1981).
- [72] J. R. Hart, A. K. Rappe, S. M. Gorun, and T. H. Upton, *Inorg. Chem.* **31**, 5254 (1992).
- [73] A. Caneschi, F. Fabrizi de Biani, L. Kloof, and P. Zanello, *Int. J. Quantum Chem.* **72**, 61 (1999).
- [74] Z. Chen, Z. Xu, L. Zhang, F. Yan, and Z. Lin, *J. Phys. Chem. A* **105**, 9710 (2001).
- [75] A. I. Ermakov, I. V. Yurova, A. D. Davydov, B. A. Khorishko, A. P. Lar'kov, and K. V. Stanislavchik, *Russ. J. Gen. Chem.* **83**, 1493 (2013).
- [76] M. Friák, A. Schindlmayr, and M. Scheffler, *New J. Phys.* **9**, 5 (2007).
- [77] A. J. A. Aquino, D. Tunega, G. Haberhauer, M. H. Gerzabek, and H. Lischka, *J. Phys. Chem. C* **111**, 877 (2007).
- [78] I. Bernal-Villamil and S. Gallego, *J. Phys.: Condens. Matter* **27**, 012001 (2015).
- [79] M. Mahmoudi, A. Simchi, M. Imani, A. S. Milani, and P. Stroeve, *J. Phys. Chem. B* **112**, 14470 (2008).
- [80] Y. Tian, B. Yu, X. Li, and K. Li, *J. Mater. Chem.* **21**, 2476 (2011).
- [81] O. A. Attallah, M. A. Al-Ghobashy, M. Nebsen, and M. Y. Salem, *RSC Adv.* **6**, 11461 (2016).
- [82] G. Sharma and P. Jeevanandam, *RSC Adv.* **3**, 189 (2013).
- [83] S. A. Jadhav and S. V. Patil, *Front. Mater. Sci.* **8**, 193 (2014).
- [84] S. R. Elliott, *Physics of Amorphous Materials*, (Longman Scientific & Technical, Harlow, Essex, England, 1990).
- [85] R. M. Cornell and U. Schwertmann, in *The Iron Oxides: Structure, Properties, Reactions, Occurrences and Uses*, 2nd Ed. (Wiley-VCH Verlag GmbH & Co. KGaA, 2004), p. 111.
- [86] *10993-5 Biological Evaluation of Medical Devices – Part 5: Tests for in vitro Cytotoxicity*, 10993-5 (ISO: Geneva, Switzerland, 2009).
- [87] G. Huang, H. Chen, Y. Dong, X. Luo, H. Yu, Z. Moore, E. A. Bey, D. A. Boothman, and J. Gao, *Theranostics* **3**, 116 (2013).
- [88] P. Sanganeria, S. Sachar, S. Chandra, D. Bahadur, P. Ray, and A. Khanna, *J. Biomed. Mater. Res. B* **103**, 125 (2015).